NANO LETTERS

pubs.acs.org/NanoLett Letter

Observation of Bloch Flatbands and Localized States in Moiré Bilayer Grating

Qinyu Jing,[#] Zhiyuan Che,[*,#] Shaohu Chen, Tongtong Xue, Jiajun Wang, Wenzhe Liu, Yunyun Dai, Lei Shi,[*] and Jian Zi[*]

Cite This: https://doi.org/10.1021/acs.nanolett.5c00304 Read Online

ACCESS | Metrics & More | Article Recommendations | Supporting Information

ABSTRACT: Here, we explore the formation of Bloch flatbands in photonic moiré bilayer grating. The stacking-induced interlayer coupling contrast serves as a crucial condition for flatband formation. The number of Bloch flatbands is related to the number of antinodes present within one unitcell of monolayer grating. By applying the band-unfolding approach to moiré supercell states, we identify that the associated localized states in moiré bilayer grating arise from the "beating" mode between Bloch standing-waves associated with two similar periods. Experimentally, we established a resonance-enhanced photon scattering setup to directly measure Bloch flatbands and observe the corresponding localized states in the moiré photonic system. Furthermore, we present the experimental demonstration of third-harmonic generation enhancement facilitated by moiré-induced flatbands. Our work provides insights into moiré-induced modulation of photonic band structures, opening up possibilities for novel optical phenomena and device applications in photonic crystals.

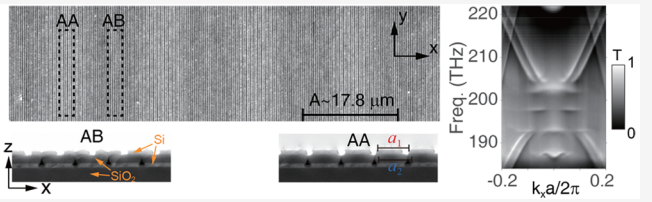

KEYWORDS: *moiré bilayer grating, Bloch flatband, localized state, nonlinear enhancement*

Van der Waals materials have recently garnered significant attention for their unique properties, including correlated insulator, superconducting, and topological states.[1−5] A notable example is twisted bilayer graphene, garnering widespread interest for its flatbands with a magic-angle.[6−9] These paired flatbands near the Fermi level arise from the interference of Dirac cones, known as Dirac flatbands.[9] Beyond twisted bilayer graphene, moiré superlattices from alternative two-dimensional materials like transition metal dichalcogenides and hexagonal boron nitride also form flatbands.[10−15] Unlike twisted bilayer graphene, their flatbands arise from Bloch standing-wave interference at the bandgap edge, termed Bloch flatbands.[13,15] The Bloch flatband mechanism provides unique advantages, such as the formation of multiple flatbands without a specific magic-angle.

Inspired by the intriguing coupling behavior in van der Waals materials, the moiré superlattice concept has been transposed into photonic systems. This infusion of moiré-inspired tunability has spurred significant advancements in both theoretical exploration[16−26] and practical applications.[27−32] A theoretical development introduced the concept of a "magic-distance", exploiting the tunable interlayer spacing in photonic systems to achieve Bloch flatbands—analogous to the magic-angle in bilayer graphene.[23] One notable application is the moiré nanolaser, which leverages photonic flatbands in twisted photonic graphene superlattices.[27,32] Collectively, these studies underscore the unparalleled tunability of photonic systems, opening new pathways for investigating novel physical phenomena and applications in moiré superlattices.

In this Letter, we theoretically analyze and experimentally observe the formation of Bloch flatbands in moiré bilayer gratings (MBGs). We elucidate that interlayer coupling contrast originates from the overlap of Bloch standing-wave antinodes within each layer, establishing a direct relationship between the number of antinodes within a monolayer grating unitcell and the quantity of possible flatbands. Bloch flatbands with localized wave functions are generated when the eigenfrequencies of strongly interlayer-coupled modes fall within the bandgap of weakly interlayer-coupled stacking. Utilizing the band-unfolding approach, we quantify the contribution weights of each monolayer grating for a specific moiré supercell mode, attributing localized states in MBG to the "beating" mode of Bloch standing-waves associated with two distinct periods. As a practical application of moiré-induced flatbands, we experimentally measure the enhancement of third-harmonic generation.

We first analyze interlayer coupling contrast in different stacking regions of photonic moiré bilayer structures. In Figure

Received: January 14, 2025
Revised: February 24, 2025
Accepted: February 27, 2025

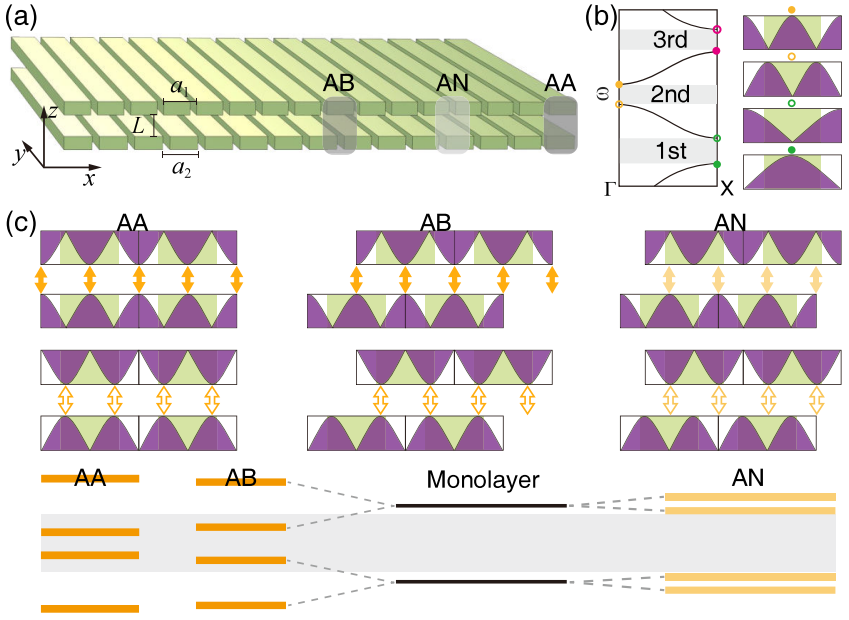

Figure 1. Stacking-induced interlayer coupling contrast. (a) Schematic of a moiré bilayer grating with AA- and AB-stackings. (b) Band structure of monolayer grating and Bloch modes at the bandgap edge. Energy profiles along the *x*-direction within one unitcell show varying antinodes at different bandgap edges. (c) Interlayer coupling for second bandgap edge modes. AA- and AB-stackings, with aligned upper and lower layer antinodes, exhibit stronger interlayer coupling and larger band splitting, while AN-stacking, with aligned antinodes and nodes, displays weaker interlayer coupling and smaller band splitting.

1(a), we depict a one-dimensional MBG, consisting of two-layer gratings with interlayer spacing and mismatched lattices. Lattice mismatch generates moiré patterns, forming periodic supercells with distinct stacking regions—aligned AA-stacking and misaligned AB-stacking with a half-period offset (Figure 1(a)). Different stacking configurations typically exhibit varying interlayer coupling strengths.[23,33] To illustrate this, we examine a monolayer grating and two identical gratings stacked with a fixed interlayer spacing. Figure 1(b) (left) shows a schematic of the band structure along the Γ−X direction for a monolayer grating, indicating directional bandgaps with gray shaded regions. Bloch modes at the bandgap edges are standing waves, displaying alternating antinodes and nodes. Energy profiles along the *x*-direction within one unitcell exhibit varying antinode/node configurations, depending on the bandgap order (right panel of Figure 1(b)).

Figure 1(c) schematically illustrates interlayer couplings for Bloch modes at the second bandgap edge. In AA-stacking, modes' antinodes align, resulting in substantial field overlap and stronger interlayer coupling (deep yellow arrows). Similarly, AB-stacking shows antinode alignment due to its half-period offset, also indicating stronger coupling. Conversely, AN-stacking (quarter-period offset) displays minimal field overlap, indicating weaker interlayer coupling (light yellow arrows). Solid (hollow) arrows correspond to modes represented by yellow solid circles in Figure 1(b). Further insights into interlayer coupling differences between AA-, AB-, and AN-stackings are provided using energy-level diagrams in the lower panel of Figure 1(c). The energy levels of interlayer-coupled Bloch modes in these stackings can be viewed as the splitting of levels derived from the monolayer grating. Stronger interlayer coupling results in a larger splitting, while weaker interlayer coupling leads to a smaller splitting, inheriting the directional bandgap from the monolayer grating.

The significant contrast results in four strongly interlayer-coupled Bloch modes (middle energy levels) of AA- and AB-stackings falling within AN-stacking's bandgap (gray shaded region in Figure 1(c)). In other words, introducing AA-stacking or AB-stacking as a defect within AN-stacking structures can create two localized defect-like states in the AA-stacking or AB-stacking regions, corresponding to flatbands within the AN-stacking bandgap (see Figure S3 in the Supporting Information[34]). This key insight suggests that the contrast in interlayer couplings within different stacking regions of the MBG is crucial for forming flatbands in bilayer structures. A similar analysis applies to the first- and higher-order bandgap edges with one or more antinodes (see Figure S2), further supporting this insight. It also reveals that the number of antinodes within a unitcell of the monolayer grating intrinsically determines the number of Bloch flatbands.

In practical MBGs, regions with stronger and weaker interlayer coupling involve gratings with mismatched lattice parameters, a_1 and a_2, rather than identical gratings. We consider MBGs satisfying $a_1/a_2 = N/(N+1)$ for a natural number N.[23] The supercell period is determined by $A = (N+1)a_1 = Na_2$, where $a_{1,2} = a \mp \delta a$ with lattice mismatch $\delta a = a/(2N+1)$. This mismatch disrupts the precise alignment of antinodes and nodes within weakly interlayer-coupled stackings, resulting in increased interlayer coupling and reduced bandgap width. Consequently, the formation of sufficient flatbands for Bloch modes in strongly interlayer-coupled stackings is affected. Building on the clarifying and comprehensive effective Hamiltonian model for MBGs proposed in ref 23, a quantitative analysis of the effect of lattice mismatch on flatband formation is provided in the Supporting Information.[34]

We elucidate below the formation of Bloch flatbands in MBGs through simulations. The simulation parameters are lattice constant a = 700 nm, thickness of 100 nm, interlayer spacing L = 220 nm, refractive index of 3.6 with filling ratio 0.8, and background refractive index 1.5. For MBGs, eigenmodes and bands are simulated by using supercell calculations. To

https://doi.org/10.1021/acs.nanolett.5c00304
Nano Lett. XXXX, XXX, XXX−XXX

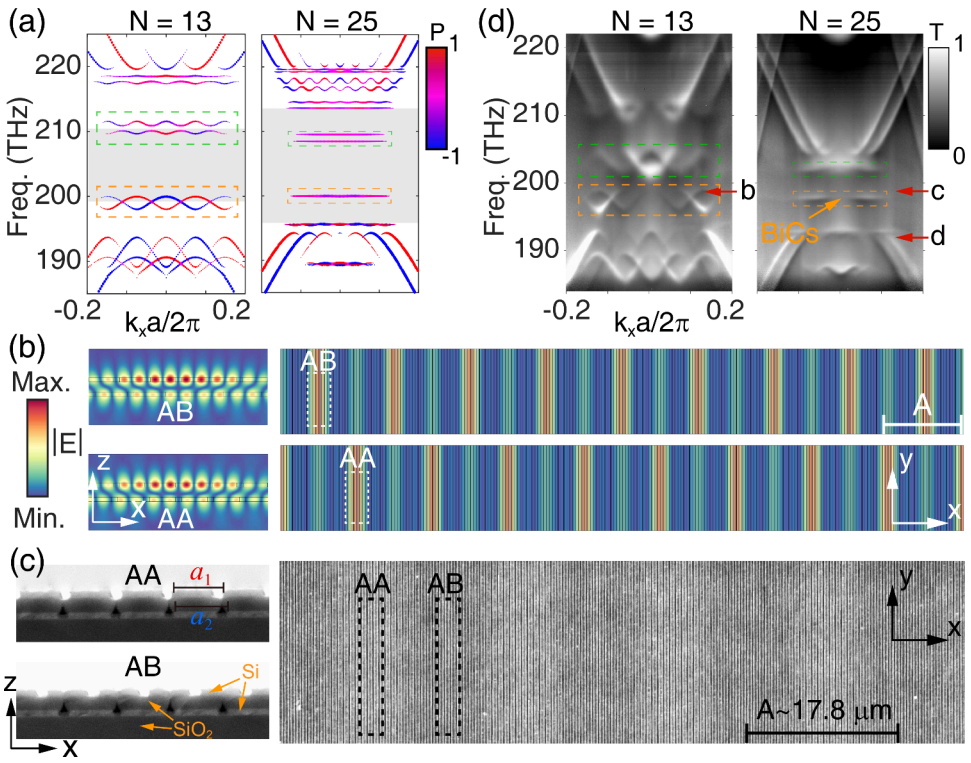

Figure 2. Flatbands and localized states of MBGs. (a) Unfolded dispersion of TE-like modes for $N = 13$ and $N = 25$ MBGs, annotated with periodicity contrast P. For the $N = 13$ sample, $A = 13a_2$, $a_2 \sim 726$ nm; for the $N = 25$ sample, $A = 25a_2$, $a_2 \sim 714$ nm. (b) Field profiles of two localized states at $k_x = 0$ in AA- and AB-stacking configurations, corresponding to the two flatbands for $N = 25$ MBG. (c) SEM image of the $N = 25$ MBG, highlighting the moiré pattern (top view) and cross-sectional views showing AA- and AB-stacking configurations. (d) Measured dispersions of MBGs for $N = 13$ and $N = 25$, showing isolated flatbands within the bandgap.

directly compare the band structures obtained from simulation and measurement of MBGs, we employ the band-unfolding approach,[35−42] mapping supercell bands onto the monolayer Brillouin zone with $k_x \in [-\pi/a, \pi/a]$. Additionally, within this framework, we introduce a periodicity contrast to quantify the contribution weights of two distinct periodic grating layers to a specific moiré supercell mode. The periodicity contrast, P, is defined by

$$P(k_x) = \frac{P_1 - P_2}{P_1 + P_2} \tag{1}$$

where $P = 1(-1)$ indicates a supercell mode is completely contributed by the $a_1(a_2)$ layer mode. P_i with $i = 1, 2$ represents the periodicity weight of a_i in a supercell state

$$P_i(k_x) = \sum_m \left| \int u_K(x) e^{-i(G_l + g_m^{(i)})x} \, dx \right|^2 \tag{2}$$

where $u_K(x)$ is the amplitude of the supercell modes and $K \in [-\pi/A, \pi/A]$ is a wavevector within the supercell Brillouin zone. $g_m^{(i)} = m2\pi/a_i$ is the reciprocal lattice vector of the a_i layer grating, while $G_l = l2\pi/A$ is the reciprocal lattice vector of the moiré supercell. m and l are arbitrary integers.[34]

The unfolded dispersions of MBGs for $N = 13$ and $N = 25$ are presented in Figure 2(a). For the $N = 13$ MBG, two pairs of intertwined bands appear near the edge of the AN-stacking bandgap (gray shaded region), approaching flatband characteristics. In contrast, for $N = 25$, four flatbands emerge within the AN-stacking bandgap. This behavior can be attributed to the effect of lattice mismatch modulation on the AN-stacking bandgap. Further discussion is provided in Figures S5 and S10.[34] By comparing the unfolded dispersion of MBGs with band structures of bilayer gratings, we highlight that pronounced interlayer coupling contrast in MBGs primarily occurs near the Γ- and X-points, where Bloch standing waves exhibit near-zero group velocity (see Figure S6). In this perspective, localized states corresponding to Bloch flatbands can be interpreted as "beating" modes between Bloch standing-waves of two gratings with close lattice constants. The colors of the flatbands in Figure 2(a), representing periodicity contrast P, indicate that these states result from the strong hybridization of Bloch standing-waves. The localization positions coincide with the antinode alignment of Bloch standing-waves, corresponding to either AA-stacking or AB-stacking. In Figure 2(b), we present the field profiles of the two flatbands for $N = 25$, showing localization in the AA-stacking and AB-stacking regions.

To experimentally validate the theoretical analyses and numerical simulations, we fabricated MBGs composed of two silicon thin-film layers with grating patterns. The intervening layer was a silicon dioxide film grown through plasma-enhanced chemical vapor deposition. The fabrication involved multiple electron-beam lithography and reactive ion etching techniques. See the Supporting Information for fabrication details.[34] The SEM image of $N = 25$ MBG and cross-sectional views of AA- and AB-stacking are shown in Figure 2(c). Experimental measurements were conducted using a home-made momentum-space imaging spectroscopy system for capturing band structures or dispersions via angle-resolved transmission spectroscopy.[43,44] Figure 2(d) shows the measured dispersions of MBGs for $N = 13$ and $N = 25$, which align well with the unfolded dispersions in Figure 2(a).

https://doi.org/10.1021/acs.nanolett.5c00304
Nano Lett. XXXX, XXX, XXX−XXX

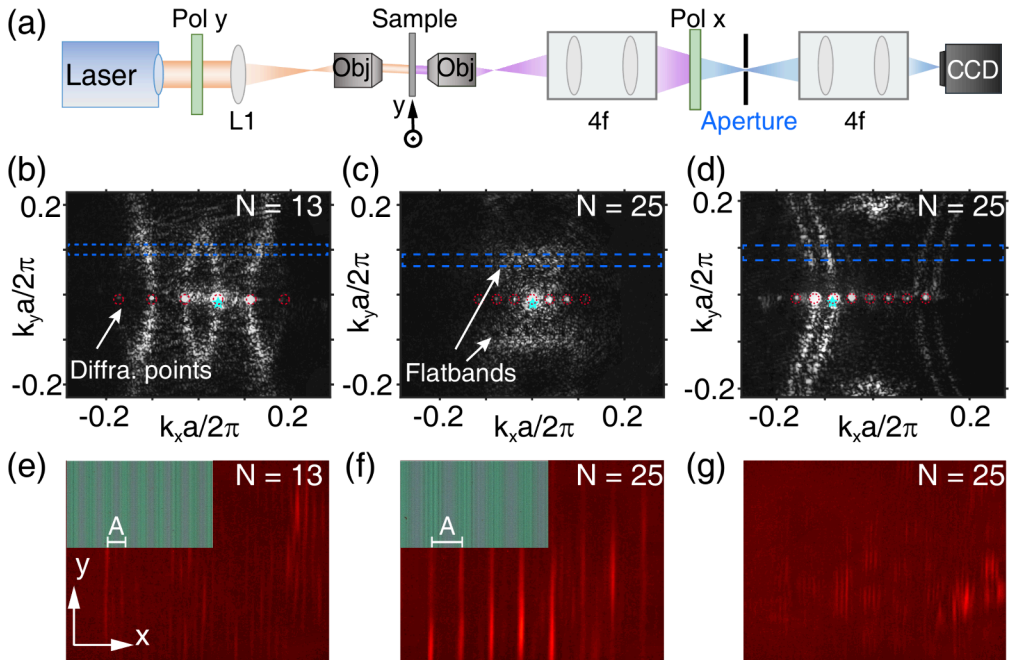

Figure 3. Observation of localized states in MBGs. (a) Schematic of the experimental setup used to measure the radiation from the guided resonances in the MBG sample. CCD, charge-coupled device; 4f, relay 4f optical system; Pol, polarizer; L, lens; Obj, objective. (b, c) Isofrequency contours of MBGs for N = 13, 25 under an excitation wavelength of 1,515 nm (red arrows in Figure 2(d)). Flatbands are observed at $k_y = \pm 0.2\pi/a$ in (c). Excitation spots are denoted by cyan stars. (e, f) Real-space images obtained through k-space filtering with a rectangular aperture (blue dashed boxes in (b) and (c)), with optical counterparts in the top-left corner. Localization in the AA-stacking regions is observed in (f). (d, g) Isofrequency contour and real-space image of N = 25 MBG from a non-flatband at 1,565 nm.

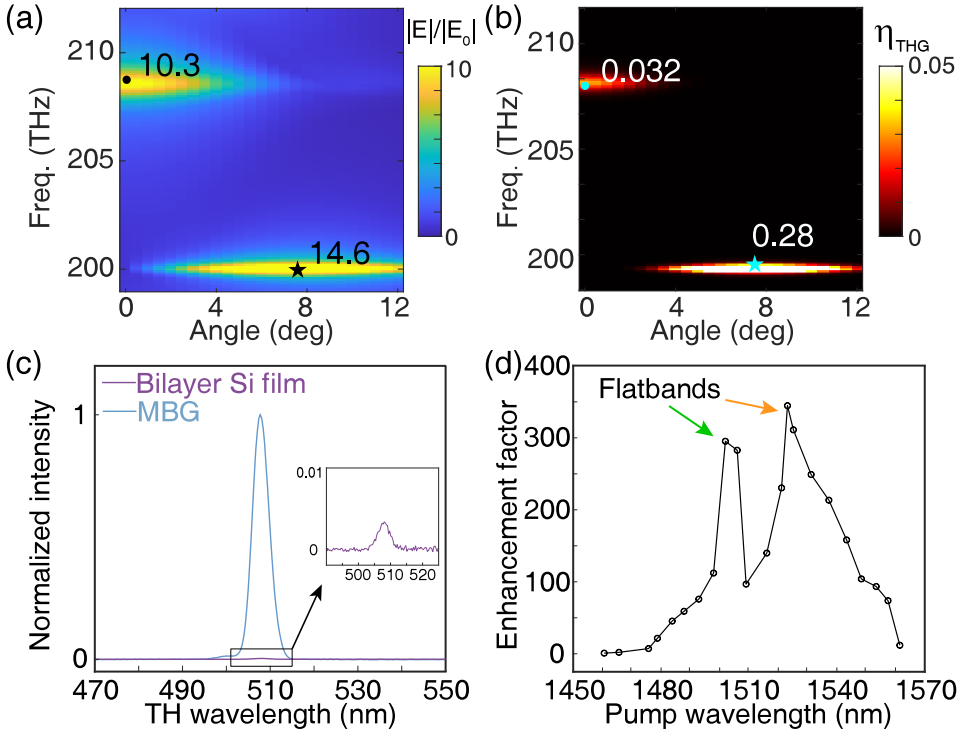

Figure 4. Enhancement of third-harmonic generation (THG) in MBG with a Bloch flatband. (a) Electric field enhancement caused by Bloch flatbands. (b) Corresponding simulated conversion efficiency of THG under Gaussian beam incidence. (c) Comparison of measured THG in MBG (N = 25) and a reference unpatterned bilayer Si film of the same thickness. (d) Dependence of THG on the pump wavelength.

For N = 13, two pairs of intertwined bands appear within the bandgap, while, for N = 25, isolated flatbands are observed. Additionally, the flatband in the N = 25 MBG shows a diminishing point at the Γ-point (orange arrow). This indicates that the mode is difficult to excite and nearly decoupled from free space, corresponding to a bound state in the continuum (BIC). BICs have been identified as singularities of far-field polarization vortices in momentum space, carrying quantized

https://doi.org/10.1021/acs.nanolett.5c00304
Nano Lett. XXXX, XXX, XXX−XXX

topological charges.[43,45,46] We employed polarization-resolved measurements to verify the presence of polarization vortices around BICs on the flatband. The extracted polarization fields reveal a vortex around the BIC with a topological charge of −1 (see Figure S19 in the Supporting Information[34]). Further symmetry analysis and simulations confirm that the BIC at the Γ-point is protected by the in-plane rotational C_2 symmetry of the MBGs. See details in the Supporting Information.[34]

The experimental observation of localized states corresponding to Bloch flatbands is unprecedented. To address this, we established an experimental setup for direct observation. The first step involves utilizing resonance-enhanced photon scattering to visualize isofrequency contours of photonic crystal samples.[47,48] When a collimated laser beam illuminates the sample, its resonance modes, matching the incident light's frequency and wavevector, are excited. Fabrication defects scatter photons into other resonance modes, possessing the same frequency but different wavevectors, reproducing isofrequency contour patterns in the far field. Subsequently, by implementing k-space filtering,[49−51] we selectively isolate the flatbands and directly image the corresponding localized states. A schematic of the experimental setup is presented in Figure 3(a).

Figures 3(b) and (c) depict momentum-space radiation maps from MBGs of N = 13 and N = 25 at an excitation wavelength of 1,515 nm (indicated by red arrows in Figure 2(d)). These maps reveal isofrequency contours, with diffraction points highlighted by red dashed circles and excitation spots indicated by cyan stars. In Figure 3(c), distinct flatbands are observable at $k_y = \pm 0.2\pi/a$. The excitation wavelength is chosen to avoid interference from diffraction points. A rectangular aperture, for filtering linear flatbands, is denoted by blue dashed boxes in Figures 3(b) and (c). Figures 3(e) and (f) depict real-space images through such rectangular aperture filtering with optical images in the top-left corner. Comparing Figures 3(e) with (f), localization is clearly observed in the AA-stacking regions of the N = 25 MBG. Figure 3(d) presents the isofrequency contours of the N = 25 MBG sample at an excitation wavelength of 1,565 nm. Unlike the flatband modes, real-space images of these non-flatband modes do not exhibit clear localization, as shown in Figure 3(g).

The moiré-induced Bloch flatband offers significant potential for various optical applications, particularly in enhancing nonlinear optical processes.[52−54] Nonlinear harmonic generation, a fundamental photon−matter interaction, can be greatly amplified by the local electromagnetic field enhancement associated with Bloch flatbands. In MBGs, substantial local field enhancement arises not only from resonance effects but also from the x-direction localization of electromagnetic modes. Figure 4(a) illustrates the simulated field enhancement for the N = 25 MBG, showing the combined contributions of resonance- and moiré-induced effects within the flatband regions, with a maximum field enhancement reaching 14.6. This pronounced field enhancement, together with the intrinsic bulk nonlinear response of Si,[55] leads to strong third-order nonlinear effects in these regions. Figure 4(b) shows the corresponding conversion efficiency of third-harmonic generation (THG) under Gaussian beam incidence with a peak amplitude of $E_0 = 5 \times 10^7$ V/m, where the maximum THG conversion efficiency reaches 0.28. Further discussions and details regarding nonlinear simulations are available in the Supporting Information.[34]

To corroborate these results, experimental measurements were conducted to validate the THG enhancement facilitated by Bloch flatbands. Figure 4(c) compares the THG from an N = 25 MBG and an unpatterned bilayer Si film of the same thickness. When pumped at resonance using a femtosecond pulsed laser (details in the Supporting Information[34]), the THG intensity from the MBG is approximately 350 times higher than that of the bare film. The link between enhanced THG and the flatband is evident from the THG's dependence on the pump wavelength, as shown in Figure 4(d). The THG enhancement factor peaks at the resonance wavelength of flatbands and decreases significantly off-resonance. Additional comparisons with THG in monolayer gratings, demonstrating at least a 5-fold enhancement by the flatband, are provided in Figure S22 of the Supporting Information.[34]

In conclusion, we have theoretically analyzed and experimentally observed the formation of Bloch flatbands and localized states in MBGs. Our work highlights the crucial role of interlayer coupling differences in distinct stacking regions for Bloch flatband formation, distinguishing it from Dirac flatbands that require specific twisted angles. Furthermore, the number of flatbands can vary based on the number of antinodes within one unitcell of the monolayer grating. The tunability of MBGs to form multiple flatbands offers versatility for various moiré-related optical applications, such as generating higher charge vortex beams,[31] nanolaser arrays,[32] enhanced free-electron radiation,[56] and optical trapping.[57] The enhancement of nonlinear third-harmonic generation facilitated by moiré-induced flatbands is observed as an illustration of their potential applications.

■ ASSOCIATED CONTENT

Supporting Information

The Supporting Information is available free of charge at https://pubs.acs.org/doi/10.1021/acs.nanolett.5c00304.

Additional details on the theoretical analysis, simulations, and experimental measurements are provided (PDF)

■ AUTHOR INFORMATION

Corresponding Authors

Zhiyuan Che − *State Key Laboratory of Surface Physics, Key Laboratory of Micro- and Nano-Photonic Structures (Ministry of Education), and Department of Physics, Fudan University, Shanghai 200433, China;* orcid.org/0000-0003-2843-1446; Email: chezy@fudan.edu.cn

Lei Shi − *State Key Laboratory of Surface Physics, Key Laboratory of Micro- and Nano-Photonic Structures (Ministry of Education), and Department of Physics, Fudan University, Shanghai 200433, China; Institute for Nanoelectronic Devices and Quantum Computing, Fudan University, Shanghai 200438, China; Shanghai Research Center for Quantum Sciences, Shanghai 201315, China; Collaborative Innovation Center of Advanced Microstructures, Nanjing University, Nanjing 210093, China;* orcid.org/0000-0001-8458-3941; Email: lshi@fudan.edu.cn

Jian Zi − *State Key Laboratory of Surface Physics, Key Laboratory of Micro- and Nano-Photonic Structures (Ministry of Education), and Department of Physics, Fudan University, Shanghai 200433, China; Institute for Nanoelectronic Devices and Quantum Computing, Fudan*

https://doi.org/10.1021/acs.nanolett.5c00304
Nano Lett. XXXX, XXX, XXX−XXX

University, Shanghai 200438, China; Shanghai Research Center for Quantum Sciences, Shanghai 201315, China; Collaborative Innovation Center of Advanced Microstructures, Nanjing University, Nanjing 210093, China; Email: jzi@fudan.edu.cn

Authors

Qinyu Jing − *State Key Laboratory of Surface Physics, Key Laboratory of Micro- and Nano-Photonic Structures (Ministry of Education), and Department of Physics, Fudan University, Shanghai 200433, China*

Shaohu Chen − *State Key Laboratory of Surface Physics, Key Laboratory of Micro- and Nano-Photonic Structures (Ministry of Education), and Department of Physics, Fudan University, Shanghai 200433, China*

Tongtong Xue − *Advanced Research Institute of Multidisciplinary Sciences, Beijing Institute of Technology, Beijing 100081, China*

Jiajun Wang − *State Key Laboratory of Surface Physics, Key Laboratory of Micro- and Nano-Photonic Structures (Ministry of Education), and Department of Physics, Fudan University, Shanghai 200433, China*; orcid.org/0000-0002-7554-370X

Wenzhe Liu − *Institute for Nanoelectronic Devices and Quantum Computing, Fudan University, Shanghai 200438, China*; orcid.org/0000-0002-6582-4161

Yunyun Dai − *School of Physics, School of Integrated Circuits and Electronics, Advanced Research Institute of Multidisciplinary Sciences, Beijing Institute of Technology, Beijing 100081, China*; orcid.org/0000-0002-1186-1864

Complete contact information is available at: https://pubs.acs.org/10.1021/acs.nanolett.5c00304

Author Contributions

#Q.J., Z.C.: Contributed equally to this work.

Notes

The authors declare no competing financial interest.

■ ACKNOWLEDGMENTS

The authors acknowledge the support of National Natural Science Foundation of China (No. 12234007, No. 12321161645, No. 12221004, and No. 62375020); National Key Research and Development Program of China (2023YFA1406900, 2022YFA1404800, and 2022YFA1403302); Major Program of National Natural Science Foundation of China (Grant No. T2394480, No. T2394481); Science and Technology Commission of Shanghai Municipality (22142200400, 21DZ1101500, 2019SHZDZX01, and 23DZ2260100); and China Postdoctoral Science Foundation (2022M720810, 2022TQ0078).

■ REFERENCES

(1) Geim, A. K.; Grigorieva, I. V. Van der Waals heterostructures. *Nature* **2013**, *499*, 419−425.

(2) Novoselov, K. S.; Mishchenko, A.; Carvalho, A.; Neto, A. H. C. 2D materials and van der Waals heterostructures. *Science* **2016**, *353*, aac9439.

(3) Carr, S.; Fang, S.; Kaxiras, E. Electronic-structure methods for twisted moiré layers. *Nat. Rev. Mater.* **2020**, *5*, 748−763.

(4) Andrei, E. Y.; MacDonald, A. H. Graphene bilayers with a twist. *Nat. Mater.* **2020**, *19*, 1265−1275.

(5) Kennes, D. M.; Claassen, M.; Xian, L.; Georges, A.; Millis, A. J.; Hone, J.; Dean, C. R.; Basov, D.; Pasupathy, A. N.; Rubio, A. Moiré heterostructures as a condensed-matter quantum simulator. *Nat. Phys.* **2021**, *17*, 155−163.

(6) Bistritzer, R.; MacDonald, A. H. Moiré bands in twisted double-layer graphene. *Proc. Natl. Acad. Sci. U.S.A.* **2011**, *108*, 12233−12237.

(7) Cao, Y.; Fatemi, V.; Demir, A.; Fang, S.; Tomarken, S. L.; Luo, J. Y.; Sanchez-Yamagishi, J. D.; Watanabe, K.; Taniguchi, T.; Kaxiras, E.; Ashoori, R. C.; Jarillo-Herrero, P. Correlated insulator behaviour at half-filling in magic-angle graphene superlattices. *Nature* **2018**, *556*, 80−84.

(8) Cao, Y.; Fatemi, V.; Fang, S.; Watanabe, K.; Taniguchi, T.; Kaxiras, E.; Jarillo-Herrero, P. Unconventional superconductivity in magic-angle graphene superlattices. *Nature* **2018**, *556*, 43−50.

(9) Tarnopolsky, G.; Kruchkov, A. J.; Vishwanath, A. Origin of Magic Angles in Twisted Bilayer Graphene. *Phys. Rev. Lett.* **2019**, *122*, 106405.

(10) Naik, M. H.; Jain, M. Ultraflatbands and Shear Solitons in Moiré Patterns of Twisted Bilayer Transition Metal Dichalcogenides. *Phys. Rev. Lett.* **2018**, *121*, 266401.

(11) Wu, F.; Lovorn, T.; Tutuc, E.; MacDonald, A. H. Hubbard Model Physics in Transition Metal Dichalcogenide Moiré Bands. *Phys. Rev. Lett.* **2018**, *121*, 026402.

(12) Xian, L.; Kennes, D. M.; Tancogne-Dejean, N.; Altarelli, M.; Rubio, A. Multiflat Bands and Strong Correlations in Twisted Bilayer Boron Nitride: Doping-Induced Correlated Insulator and Superconductor. *Nano Lett.* **2019**, *19*, 4934−4940.

(13) Zhao, X.-J.; Yang, Y.; Zhang, D.-B.; Wei, S.-H. Formation of Bloch Flat Bands in Polar Twisted Bilayers without Magic Angles. *Phys. Rev. Lett.* **2020**, *124*, 086401.

(14) Ochoa, H.; Asenjo-Garcia, A. Flat Bands and Chiral Optical Response of Moiré Insulators. *Phys. Rev. Lett.* **2020**, *125*, 037402.

(15) Tao, S.; Zhang, X.; Zhu, J.; He, P.; Yang, S. A.; Lu, Y.; Wei, S.-H. Designing Ultra-flat Bands in Twisted Bilayer Materials at Large Twist Angles: Theory and Application to Two-Dimensional Indium Selenide. *J. Am. Chem. Soc.* **2022**, *144*, 3949−3956.

(16) Fu, Q.; Wang, P.; Huang, C.; Kartashov, Y. V.; Torner, L.; Konotop, V. V.; Ye, F. Optical soliton formation controlled by angle twisting in photonic moiré lattices. *Nat. Photonics* **2020**, *14*, 663−668.

(17) Wang, P.; Zheng, Y.; Chen, X.; Huang, C.; Kartashov, Y. V.; Torner, L.; Konotop, V. V.; Ye, F. Localization and delocalization of light in photonic moiré lattices. *Nature* **2020**, *577*, 42−46.

(18) Chen, J.; Lin, X.; Chen, M.; Low, T.; Chen, H.; Dai, S. A perspective of twisted photonic structures. *Appl. Phys. Lett.* **2021**, *119*, 240501.

(19) Dong, K.; Zhang, T.; Li, J.; Wang, Q.; Yang, F.; Rho, Y.; Wang, D.; Grigoropoulos, C. P.; Wu, J.; Yao, J. Flat Bands in Magic-Angle Bilayer Photonic Crystals at Small Twists. *Phys. Rev. Lett.* **2021**, *126*, 223601.

(20) Lou, B.; Zhao, N.; Minkov, M.; Guo, C.; Orenstein, M.; Fan, S. Theory for Twisted Bilayer Photonic Crystal Slabs. *Phys. Rev. Lett.* **2021**, *126*, 136101.

(21) Tang, H.; Du, F.; Carr, S.; DeVault, C.; Mello, O.; Mazur, E. Modeling the optical properties of twisted bilayer photonic crystals. *Light Sci. Appl.* **2021**, *10*, 157.

(22) Oudich, M.; Su, G.; Deng, Y.; Benalcazar, W.; Huang, R.; Gerard, N. J. R. K.; Lu, M.; Zhan, P.; Jing, Y. Photonic analog of bilayer graphene. *Phys. Rev. B* **2021**, *103*, 214311.

(23) Nguyen, D. X.; Letartre, X.; Drouard, E.; Viktorovitch, P.; Nguyen, H. C.; Nguyen, H. S. Magic configurations in moiré superlattice of bilayer photonic crystals: Almost-perfect flatbands and unconventional localization. *Phys. Rev. Res.* **2022**, *4*, L032031.

(24) Wang, H.; Ma, S.; Zhang, S.; Lei, D. Intrinsic superflat bands in general twisted bilayer systems. *Light Sci. Appl.* **2022**, *11*, 159.

(25) Huang, L.; Zhang, W.; Zhang, X. Moiré Quasibound States in the Continuum. *Phys. Rev. Lett.* **2022**, *128*, 253901.

(26) Qin, H.; Chen, S.; Zhang, W.; Zhang, H.; Pan, R.; Li, J.; Shi, L.; Zi, J.; Zhang, X. Optical moiré bound states in the continuum. *Nat. Commun.* **2024**, *15*, 9080.

(27) Mao, X.-R.; Shao, Z.-K.; Luan, H.-Y.; Wang, S.-L.; Ma, R.-M. Magic-angle lasers in nanostructured moiré superlattice. *Nat. Nanotechnol.* **2021**, *16*, 1099.
(28) Guo, C.; Guo, Y.; Lou, B.; Fan, S. Wide wavelength-tunable narrow-band thermal radiation from moiré patterns. *Appl. Phys. Lett.* **2021**, *118*, 131111.
(29) Tang, H.; Ni, X.; Du, F.; Srikrishna, V.; Mazur, E. On-chip light trapping in bilayer moiré photonic crystal slabs. *Appl. Phys. Lett.* **2022**, *121*, 231702.
(30) Tang, H.; Lou, B.; Du, F.; Zhang, M.; Ni, X.; Xu, W.; Jin, R.; Fan, S.; Mazur, E. Experimental probe of twist angle-dependent band structure of on-chip optical bilayer photonic crystal. *Sci. Adv.* **2023**, *9*, eadh8498.
(31) Zhang, T.; Dong, K.; Li, J.; Meng, F.; Li, J.; Munagavalasa, S.; Grigoropoulos, C. P.; Wu, J.; Yao, J. Twisted moiré photonic crystal enabled optical vortex generation through bound states in the continuum. *Nat. Commun.* **2023**, *14*, 6014.
(32) Luan, H.-Y.; Ouyang, Y.-H.; Zhao, Z.-W.; Mao, W.-Z.; Ma, R.-M. Reconfigurable moiré nanolaser arrays with phase synchronization. *Nature* **2023**, *624*, 282−288.
(33) Nguyen, H. S.; Dubois, F.; Deschamps, T.; Cueff, S.; Pardon, A.; Leclercq, J. L.; Seassal, C.; Letartre, X.; Viktorovitch, P. Symmetry Breaking in Photonic Crystals: On-Demand Dispersion from Flatband to Dirac Cones. *Phys. Rev. Lett.* **2018**, *120*, 066102.
(34) See the Supporting Information.
(35) Boykin, T. B.; Klimeck, G. Practical application of zone-folding concepts in tight-binding calculations. *Phys. Rev. B* **2005**, *71*, 115215.
(36) Boykin, T. B.; Kharche, N.; Klimeck, G.; Korkusinski, M. Approximate bandstructures of semiconductor alloys from tight-binding supercell calculations. *J. Phys.: Condens. Matter* **2007**, *19*, 036203.
(37) Popescu, V.; Zunger, A. Extracting E versus $\vec{k}$ effective band structure from supercell calculations on alloys and impurities. *Phys. Rev. B* **2012**, *85*, 085201.
(38) Medeiros, P. V. C.; Stafström, S.; Björk, J. Effects of extrinsic and intrinsic perturbations on the electronic structure of graphene: Retaining an effective primitive cell band structure by band unfolding. *Phys. Rev. B* **2014**, *89*, 041407.
(39) Nishi, H.; Matsushita, Y. I.; Oshiyama, A. Band-unfolding approach to moiré-induced band-gap opening and Fermi level velocity reduction in twisted bilayer graphene. *Phys. Rev. B* **2017**, *95*, 085420.
(40) Matsushita, Y. I.; Nishi, H.; Iwata, J. I.; Kosugi, T.; Oshiyama, A. Unfolding energy spectra of double-periodicity two-dimensional systems: Twisted bilayer graphene and MoS_2 on graphene. *Phys. Rev. Mater.* **2018**, *2*, 010801.
(41) Che, Z.; Zhang, Y.; Liu, W.; Zhao, M.; Wang, J.; Zhang, W.; Guan, F.; Liu, X.; Liu, W.; Shi, L.; Zi, J. Polarization Singularities of Photonic Quasicrystals in Momentum Space. *Phys. Rev. Lett.* **2021**, *127*, 043901.
(42) Zhang, Y.; Che, Z.; Liu, W.; Wang, J.; Zhao, M.; Guan, F.; Liu, X.; Shi, L.; Zi, J. Unfolded band structures of photonic quasicrystals and moiré superlattices. *Phys. Rev. B* **2022**, *105*, 165304.
(43) Zhang, Y.; Chen, A.; Liu, W.; Hsu, C. W.; Wang, B.; Guan, F.; Liu, X.; Shi, L.; Lu, L.; Zi, J. Observation of Polarization Vortices in Momentum Space. *Phys. Rev. Lett.* **2018**, *120*, 186103.
(44) Wang, B.; Liu, W.; Zhao, M.; Wang, J.; Zhang, Y.; Chen, A.; Guan, F.; Liu, X.; Shi, L.; Zi, J. Generating optical vortex beams by momentum-space polarization vortices centred at bound states in the continuum. *Nat. Photonics* **2020**, *14*, 623−628.
(45) Hsu, C. W.; Zhen, B.; Lee, J.; Chua, S.-L.; Johnson, S. G.; Joannopoulos, J. D.; Soljačić, M. Observation of trapped light within the radiation continuum. *Nature* **2013**, *499*, 188.
(46) Zhen, B.; Hsu, C. W.; Lu, L.; Stone, A. D.; Soljačić, M. Topological Nature of Optical Bound States in the Continuum. *Phys. Rev. Lett.* **2014**, *113*, 257401.
(47) Shi, L.; Yin, H.; Zhu, X.; Liu, X.; Zi, J. Direct observation of isofrequency contour of surface modes in defective photonic crystals in real space. *Appl. Phys. Lett.* **2010**, *97*, 251111.
(48) Regan, E. C.; Igarashi, Y.; Zhen, B.; Kaminer, I.; Hsu, C. W.; Shen, Y.; Joannopoulos, J. D.; Soljačić, M. Direct imaging of isofrequency contours in photonic structures. *Sci. Adv.* **2016**, *2*, e1601591.
(49) St-Jean, P.; Goblot, V.; Galopin, E.; Lemaître, A.; Ozawa, T.; Le Gratiet, L.; Sagnes, I.; Bloch, J.; Amo, A. Lasing in topological edge states of a one-dimensional lattice. *Nat. Photonics* **2017**, *11*, 651−656.
(50) Jin, J.; Yin, X.; Ni, L.; Soljačić, M.; Zhen, B.; Peng, C. Topologically enabled ultrahigh-Q guided resonances robust to out-of-plane scattering. *Nature* **2019**, *574*, 501−504.
(51) Yin, X.; Jin, J.; Soljačić, M.; Peng, C.; Zhen, B. Observation of topologically enabled unidirectional guided resonances. *Nature* **2020**, *580*, 467−471.
(52) Shcherbakov, M. R.; Neshev, D. N.; Hopkins, B.; Shorokhov, A. S.; Staude, I.; Melik-Gaykazyan, E. V.; Decker, M.; Ezhov, A. A.; Miroshnichenko, A. E.; Brener, I.; Fedyanin, A. A.; Kivshar, Y. S. Enhanced Third-Harmonic Generation in Silicon Nanoparticles Driven by Magnetic Response. *Nano Lett.* **2014**, *14*, 6488−6492.
(53) Yang, Y.; Wang, W.; Boulesbaa, A.; Kravchenko, I. I.; Briggs, D. P.; Puretzky, A.; Geohegan, D.; Valentine, J. Nonlinear Fano-Resonant Dielectric Metasurfaces. *Nano Lett.* **2015**, *15*, 7388−7393.
(54) Wang, X.; Liu, Z.; Chen, B.; Qiu, G.; Wei, D.; Liu, J. Experimental Demonstration of High-Efficiency Harmonic Generation in Photonic Moiré Superlattice Microcavities. *Nano Lett.* **2024**, *24*, 11327−11333.
(55) Zhang, X.; Cao, Q.-T.; Wang, Z.; Liu, Y.-x.; Qiu, C.-W.; Yang, L.; Gong, Q.; Xiao, Y.-F. Symmetry-breaking-induced nonlinear optics at a microcavity surface. *Nat. Photonics* **2019**, *13*, 21−24.
(56) Yang, Y.; Roques-Carmes, C.; Kooi, S. E.; Tang, H.; Beroz, J.; Mazur, E.; Kaminer, I.; Joannopoulos, J. D.; Soljačić, M. Photonic flatband resonances for free-electron radiation. *Nature* **2023**, *613*, 42−47.
(57) Le, N. D.; Bouteyre, P.; Kheir-Aldine, A.; Dubois, F.; Cueff, S.; Berguiga, L.; Letartre, X.; Viktorovitch, P.; Benyattou, T.; Nguyen, H. S. Super Bound States in the Continuum on a Photonic Flatband: Concept, Experimental Realization, and Optical Trapping Demonstration. *Phys. Rev. Lett.* **2024**, *132*, 173802.

https://doi.org/10.1021/acs.nanolett.5c00304
Nano Lett. XXXX, XXX, XXX−XXX